metals

MDPI

Article

Influence of Annealing on the Microstructures and Oxidation Behaviors of $Al_8(CoCrFeNi)_{92}$, $Al_{15}(CoCrFeNi)_{85}$, and $Al_{30}(CoCrFeNi)_{70}$ High-Entropy Alloys

Todd M. Butler [1,2] and Mark L. Weaver [2,*]

[1] UES, Inc., 4401 Dayton-Xenia Road, Dayton, OH 45432-1805, USA; eternallyscience@gmail.com
[2] Department of Metallurgical and Materials Engineering, University of Alabama, Tuscaloosa, AL 35487-0202, USA
* Correspondence: mweaver@eng.ua.edu; Tel.: +1-205-348-7073

Academic Editors: Michael C. Gao and Junwei Qiao
Received: 28 July 2016; Accepted: 5 September 2016; Published: 12 September 2016

Abstract: The understanding of the oxidation behaviors of as-cast and annealed high-entropy alloys (HEAs) is currently limited. This work systematically investigates the influence of annealing on the microstructures and oxidation behaviors of AlCoCrFeNi-based HEAs. Annealing was found to alter the distribution of Al-rich phases which caused a change in the oxidation mechanisms. In general, all three of the investigated HEAs displayed some degree of transient oxidation at 1050 °C that was later followed by protective, parabolic oxide growth. The respective oxidation behaviors are discussed relative to existing oxide formation models for Ni–Cr–Al alloys.

Keywords: high-entropy; oxidation; multi-component alloys

1. Introduction

Recently, a novel class of compositionally-complex alloys termed high-entropy alloys (HEAs) have attracted substantial interest in the scientific community [1–4]. In contrast to conventional alloys, HEAs lack a primary constituent and are generally composed of five or more elements in nearly equal proportions [1,2]. It is well-known that these alloys typically form phases with simple FCC, BCC, and HCP crystal structures and can contain ordered intermetallic phases [4]. HEAs also exhibit the inherent potential to be alloyed with high concentrations of Al and/or Cr to promote enhanced oxidation resistances without necessarily forming various intermetallic phases that can be deleterious to strength [5–7]. In addition, HEAs have been reported to exhibit sluggish diffusion kinetics [8–10] and high thermal stabilities [11–13], making them ideal candidates for use in high temperature applications. However, a fundamental understanding of the active oxidation mechanisms are required in order to effectively implement HEAs in these environments.

With regard to oxidation, there have been a number of publications that have reported the oxidation behaviors of HEAs. These studies include both transition metal based [6,7,14–25] and refractory metal based [26–29] HEA systems. In general, it was reported that elements that commonly oxidize in less-complex, conventional alloy systems (i.e., Ni, Mn, Cr, Al, Ti) also tend to preferentially oxidize in compositionally complex alloys. For example, Daoud et al. [23] examined the oxidation behaviors of $Al_8Co_{17}Cr_{17}Cu_8Fe_{17}Ni_{33}$, $Al_{23}Co_{15}Cr_{23}Cu_8Fe_{15}Ni_{15}$, and $Al_{17}Co_{17}Cr_{17}Cu_{17}Fe_{17}Ni_{17}$ HEAs at 800 °C and 1000 °C in air. At 800 °C, the low Al content alloy formed a combination of NiO, Fe-oxide, Cr_2O_3, and Al_2O_3. However, at 1000 °C, the same alloy preferentially formed Cr_2O_3 above Al_2O_3. As for the other two HEAs, which contained considerably higher concentrations of Al, Al_2O_3 scales tended to form at both temperatures. Similarly, Holcomb et al. [24] investigated the

oxidation behaviors of eight model CoCrFeMnNi-based HEAs, along with various other conventional alloys. It was reported that the Cr and Mn containing HEAs preferentially formed both Cr_2O_3 and Mn oxides. This idea can also be extended to the realm of refractory HEAs. Senkov et al. [26] examined the 1000 °C oxidation behavior of an arc-melted $NbCrMo_{0.5}Ta_{0.5}TiZr$ HEA. The oxidation behavior was reported to be superior to that of similar Nb-based refractory alloys, with an oxide consisting of a combination of $NbCrO_4$, TiO_2, and Cr_2O_3. Likewise, Gorr et al. [27,28] investigated the high temperature oxidation behaviors of a 20Nb-20Mo-20Cr-20Ti-20Al HEA with and without Si additions. It was reported that in general, the HEA without Si followed a linear oxide growth rate law and formed a porous, non-protective mix of various oxides. Interestingly, a small addition of 1 at % Si promoted parabolic oxide growth kinetics, to some extent, and facilitated the formation of a thinner, nearly continuous scale with Al and Cr rich layers.

Based on the published literature on the oxidation behavior of HEAs, it is evident that they tend to oxidize in a similar manner compared to simple alloys based on the same elements. However, there are few publications that attempt to systematically correlate the oxidation behavior of HEAs with existing oxide formation models [6,7,15]. There is also lack of understanding of the influence of annealing on the active oxidation mechanisms, as most published results emphasize as-cast alloys. This work investigates the microstructures and oxidation behaviors of three AlCoCrFeNi based HEAs with various Al contents. This particular alloy system is ideal for a fundamental oxidation study since it contains both Al and Cr, which are known to produce protective Cr_2O_3 and/or Al_2O_3 scales [30]. Additionally, the AlCoCrFeNi system is one of the most thoroughly investigated to date [1,4,10,14,31–43]. This paper will systematically report the influence of annealing on the microstructures and active oxidation mechanisms. The results will be discussed relative to existing oxide formation models developed for model Ni–Cr–Al alloys [30].

2. Materials and Methods

Three bulk alloy buttons with the compositions of $Al_8(CoCrFeNi)_{92}$, $Al_{15}(CoCrFeNi)_{85}$, and $Al_{30}(CoCrFeNi)_{70}$ (designated: Al_8, Al_{15}, and Al_{30}) were arc-melted from pure elemental constituents on a water-cooled copper hearth in an inert ultra-high purity (UHP) argon atmosphere. Each button was flipped and re-melted five times to promote homogeneity. CALPHAD based thermodynamic modeling using the TCNI8 database in ThermoCalc™ was used in conjunction with microstructural analyses to select the appropriate annealing conditions [44–47]. Annealing was carried out at 1050 °C for 120 h under an inert, dynamic UHP Ar atmosphere.

The microstructures of the as-cast, annealed, and oxidized specimens were characterized using a combination of X-ray diffraction (XRD), scanning electron microscopy (SEM), transmission electron microscopy (TEM), scanning-transmission electron microscopy-high angle annular darkfield (STEM-HAADF), and energy-dispersive X-ray spectroscopy (EDS) in both SEM and TEM modes. XRD measurements were conducted on a Philips X'pert MPD XRD (Philips, Amsterdam, The Netherlands) using an accelerating voltage of 45 kV, a current of 40 mA, and a step size of 0.1 degrees. SEM images were captured at 20 kV using a spot size of 10 in a JEOL 7000F SEM (JEOL Ltd., Tokyo, Japan). Specimens for SEM were mounted in hot phenolic resin and polished using standard metallographic techniques up to a 0.05 micron finish. STEM-HAADF images and selected area diffraction patterns (SADPs) were captured on a 200-keV FEI Tecnai G^2 F-20 Supertwin scanning-transmission electron microscope. TEM samples were prepared using a variation of the focused-ion-beam (FIB) lift-out method in an FEI Quanta 200 3D Dual Beam FIB microscope (FEI Company, Hillsboro, OR, USA) [48]. Discontinuous isothermal oxidation tests of the as-cast and annealed specimens were conducted at 1050 °C in a tube furnace under ambient laboratory air. Prior to testing, specimens were ground to a 1200 grit surface finish followed by ultrasonic cleaning in acetone. Samples were periodically removed from the furnace and weighed using a microbalance (accuracy of 10^{-6} g).

3. Results and Discussion

3.1. Microstructures of the As-Cast and Annealed HEAs

Table 1 shows the bulk compositions, as measured using EDS. The actual compositions were found to be in good agreement with the intended compositions. Figure 1 shows representative microstructures for the as-cast, (a–c), and annealed, (d–f), Al_8, Al_{15}, and Al_{30} HEAs. All of the as-cast microstructures shown here are taken from [7,15]. Figure 1a shows a backscattered electron (BSE) image of the as-cast Al_8 HEA, which consisted of a bright, high atomic number contrast (high-Z), matrix with dark, low atomic number Z contrast (low-Z), interdendritic regions. Some AlN inclusions were also present and were attributed to impurities in the starting materials.

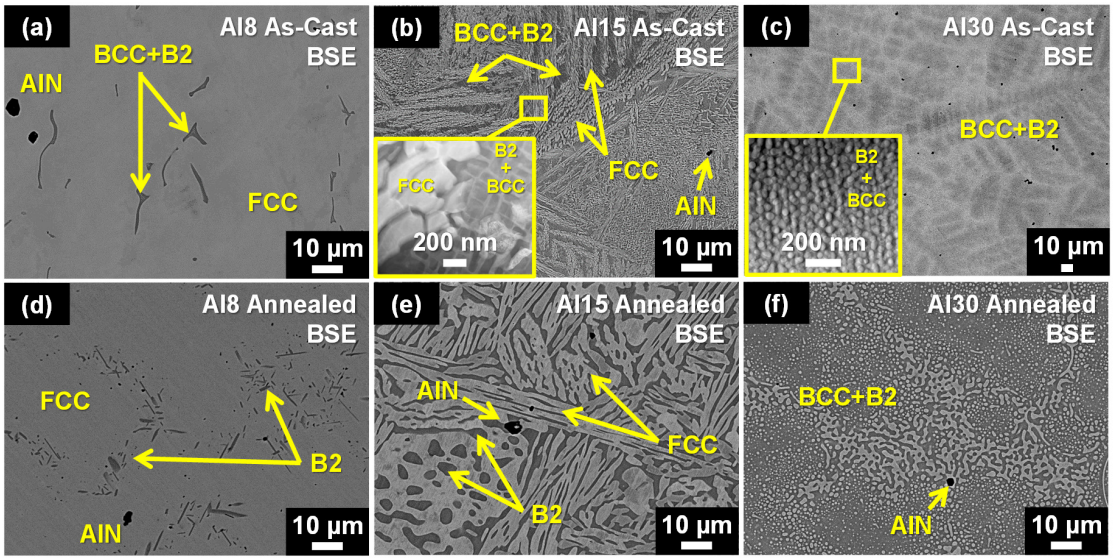

Figure 1. Representative backscattered electron (BSE) images of the Al_8, Al_{15}, and Al_{30} high-entropy alloys (HEAs) in as-cast (**a**–**c**) and annealed (**d**–**f**) conditions, respectively. The inset images in (**b**,**c**) are higher resolution scanning-transmission electron microscopy-high angle annular darkfield (STEM-HAADF) images of the Al_{15} and Al_{30} HEAs. The as-cast BSE images are taken from [7,15].

Annealing of the Al_8 HEA resulted in the decomposition of the low-Z interdendritic regions into a dense distribution of low-Z precipitates with platelet-like morphologies, as is shown in the BSE image in Figure 1d. Although not detailed here, TEM analysis was also conducted on the as-cast Al_8 HEA [7,15]. It was determined that the continuous matrix phase was FCC, while the low-Z interdendritic regions were multiphase consisting of an ordered B2 phase interspersed with high-Z BCC precipitates. The phase compositions are shown in Table 1. These BCC precipitates were not observed in the annealed Al_8 HEA. Figure 2a shows a STEM-HAADF image for the annealed Al_8 HEA. The matrix was found to have an FCC crystal structure, while the low-Z interdendritic regions were found to have a B2 crystal structure, as evident from the selected area electron diffraction patterns (SADPs) in Figure 2b,c, respectively. The B2 regions were enriched in Ni and Al, while the FCC region was Cr and Fe rich (See Table 1).

Figure 1b shows a representative BSE image and inset STEM-HAADF image for the as-cast Al_{15} HEA. The as-cast HEA consisted of colonies of high-Z contrast Widmanstätten-like lamellae and highly transformed, multiphase regions, Figure 1b. TEM analysis revealed the high-Z contrast phase to be FCC, whereas the transformed regions consisted of a BCC matrix with cuboidal B2 precipitates [7,15]. The phase chemistries are listed in Table 1. Figure 1e shows a representative BSE image for the annealed Al_{15} HEA. The annealed microstructure consisted of a semi-continuous mixture of coarsened high-Z contrast lamellae and globular regions intermixed with a discontinuous low-Z phase.

Table 1. Chemistries of the as-cast HEAs in at % (SEM-EDS). The respective phase chemistries for each as-cast HEA and after annealing for 120 h/1050 °C are also shown. ** As-cast chemistries taken from [7,15].

Alloy	Phase	Al	Ni	Co	Cr	Fe
Al_8	**Target**	8.0	23.0	23.0	23.0	23.0
	As-cast Bulk	8.2 ± 0.2	22.2 ± 0.5	22.8 ± 0.2	24.0 ± 0.3	22.8 ± 0.2
	BCC (as-cast) **	17.1 ± 0.5	22.9 ± 0.8	16.8 ± 0.4	26.7 ± 1.1	16.5 ± 0.6
	FCC (as-cast) **	10.4 ± 0.2	23.4 ± 0.1	20.8 ± 0.2	25.1 ± 0.1	20.3 ± 0.4
	FCC (*annealed*)	7.7 ± 0.2	21.9 ± 0.3	23.3 ± 0.1	24.2 ± 0.2	23.0 ± 0.3
	B2 (as-cast) **	22.5 ± 0.1	28.6 ± 0.4	16.4 ± 0.1	18.6 ± 0.4	13.9 ± 0.4
	B2 (*annealed*)	25.2 ± 2.2	21.9 ± 0.3	16.9 ± 1.0	13.0 ± 2.3	14.3 ± 1.3
Al_{15}	**Target**	15.0	21.25	21.25	21.25	21.25
	As-cast Bulk	15.6 ± 0.1	20.5 ± 0.1	20.8 ± 0.1	21.9 ± 0.1	21.1 ± 0.1
	BCC (as-cast) **	5.5 ± 1.3	21.3 ± 3.9	21.1 ± 0.3	30.8 ± 0.9	21.4 ± 2.0
	FCC (as-cast) **	12.6 ± 0.7	21.4 ± 0.7	21.5 ± 0.7	21.8 ± 0.7	21.7 ± 0.1
	FCC (*annealed*)	6.9 ± 0.2	16.5 ± 0.2	22.9 ± 0.5	28.1 ± 0.4	25.6 ± 0.5
	B2 (as-cast) **	19.7 ± 1.9	31.3 ± 3.6	21.5 ± 0.7	11.2 ± 3.6	16.5 ± 1.5
	B2 (*annealed*)	31.0 ± 0.6	29.4 ± 0.5	17.3 ± 0.4	10.0 ± 0.8	12.2 ± 0.6
Al_{30}	**Target**	30	17.5	17.5	17.5	17.5
	As-cast Bulk	29.2 ± 0.2	17.4 ± 0.1	17.6 ± 0.1	18.3 ± 0.1	17.6 ± 0.2
	BCC (as-cast) **	17.2 ± 0.5	13.2 ± 1.4	16.3 ± 1.9	29.3 ± 2.2	24.1 ± 1.7
	BCC (*annealed*)	11.7 ± 0.3	6.0 ± 0.7	13.3 ± 0.2	40.6 ± 0.1	28.2 ± 0.4
	B2 (as-cast) **	32.2 ± 0.7	25.9 ± 0.2	24.1 ± 0.7	4.6 ± 0.4	13.1 ± 0.1
	B2 (*annealed*)	35.5 ± 1.3	20.4 ± 0.9	18.2 ± 0.8	12.0 ± 2.1	13.9 ± 0.8

Figure 2b shows a STEM-HAADF image collected from the annealed Al_{15} HEA. The high-Z, semi-continuous matrix was found to have an FCC crystal structure, while the low-Z regions had B2 crystal structures, as can be seen evident in the SADPs in Figure 2e,f. No precipitates were visually evident within the B2 phase. However, extra reflections were observed in the SADP, indicating the possibility of a nanoscale phase, Figure 2f. Like in the annealed Al_8 HEA, the FCC phase was found to be Cr and Fe rich, while the B2 phase was found to be Ni and Al rich (see Table 1).

Figure 1c shows a representative BSE image and inset STEM-HAADF image for the as-cast Al_{30} HEA. Remnants of dendritic segregation are evident in the BSE image. However, STEM-HAADF imaging revealed the entire microstructure to be composed of a fine-scale distribution of high-Z contrast precipitates with BCC crystal structures dispersed in a low-Z contrast B2 matrix [7,15]. The as-cast phase chemistries are shown in Table 1.

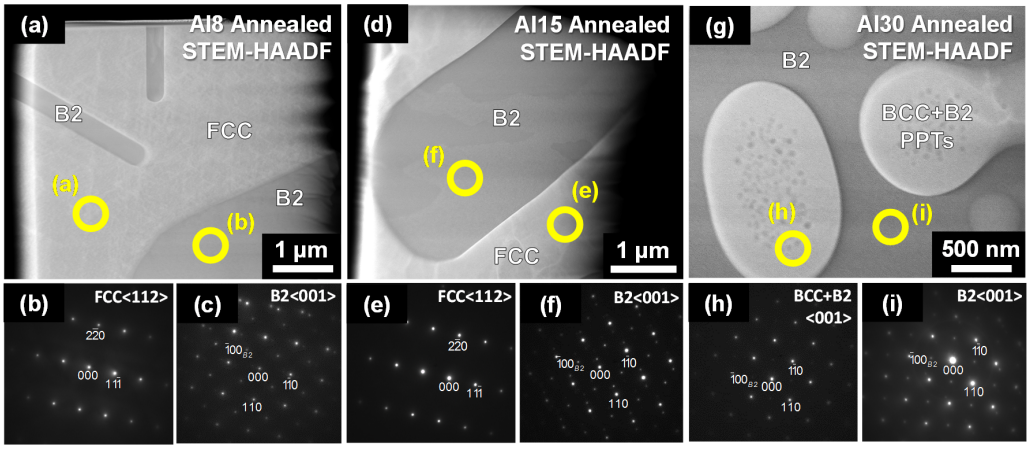

Figure 2. STEM-HAADF images and corresponding selected area diffraction patterns (SADPs) for the annealed Al_8 (**a**–**c**); Al_{15} (**d**–**f**); and Al_{30} (**g**–**i**) HEAs. The open circles indicate the locations from which the SADPs were collected.

Similar BCC+B2 microstructures have been reported in as-cast HEAs with similar compositions by Wang et al. [32,35,39]. Similar to the Al_{15} HEA, annealing caused significant coarsening of the microstructure. Figure 1f shows a BSE image of the annealed Al_{30} HEA, which consisted of an apparent mixture high-Z contrast and low-Z contrast regions. TEM analysis was conducted on the annealed Al_{30} HEA (Figure 2g). The low-Z contrast regions were found to be precipitate-free, with a B2 crystal structure that was Ni and Al rich, Figure 2i and Table 1. The high-Z contrast regions were found to be composed of two phases; a high-Z contrast matrix phase with a BCC structure that was Cr and Fe rich and a lower-Z contrast precipitate phase with a B2 crystal structure, Figure 2g,h. Differentiation between the two crystal structures (BCC matrix and B2 precipitate) was determined by observing the $<001>_{B2}$ || $<001>_{BCC}$ and $<011>_{B2}$ || $<011>_{BCC}$ SADPs near the centers and outer edges of the high-Z phase. Near the center, which contained a large number of precipitates, the diffraction patterns contained clear superlattice reflections that were consistent with $(100)_{B2}$ reflections. However, diffraction patterns taken near the outer edges of the high-Z phase, which was precipitate free, had no superlattice reflections inferring that the high-Z phase is BCC and that the precipitates are B2.

To better elucidate the phase evolution in each HEA post annealing, experimental phase fractions were determined using two-dimensional image contrast thresholding. The phases were sorted based on their particular contrast and segmented to determine a respective area phase fraction. This was then converted into a three-dimensional value assuming an equivalent spherical radius [49]. The results are shown in Table 2 along with the thermodynamically predicted phase fractions. In the Al_8 and Al_{15} HEAs, the annealing process appears to have destabilized the BCC phase, as indicated by a decrease in the respective phase fractions. This observation is consistent with the thermodynamic predictions which showed no BCC phase to be stable at the 1050 °C annealing temperature. In general, the estimated phase fractions for the annealed HEAs were found to be reasonably accurate. It is also important to note that the phase chemistries for the as-cast HEAs, reported in [7,15], were not significantly different from the corresponding phases in the annealed condition. This infers that annealing does not significantly alter the phase chemistries, but does tend to change the phase size and morphology. The phase fraction of B2 increased for all of the HEAs after annealing.

Table 2. Respective phases from each HEA along with the estimated phase fractions for the as-cast and annealed states. For comparison, the thermodynamically predicted phase fractions (at 1050 °C) as predicted from ThermoCalc are also shown.

Alloy	Phase	Estimated (2D) Phase Fraction (%) As-Cast	Estimated (2D) Phase Fraction (%) Annealed	Phase Fraction (%) Thermo-Calc™ (at 1050 °C)
Al_8	**FCC**	98	89	88
	BCC	0.76	—	—
	B2	1.24	11	12
Al_{15}	**FCC**	54	59	53
	BCC	26	—	—
	B2	20	41	47
Al_{30}	**BCC**	39	29	21
	B2	61	71	79

3.2. Oxidized Microstructures

Figure 3 shows representative BSE images of the as-cast and annealed HEAs after 50 h of oxidation at 1050 °C. In contrast to the as-cast HEAs [7,15], all of the annealed HEAs exhibited higher degrees of scale spallation. Oxidation of the as-cast Al_8 HEA resulted in the formation of an outer Cr_2O_3 scale, along with a sublayer of oxygen-enriched alloy (labeled "metal") atop an internal, semi-continuous Al_2O_3 scale, Figure 3a,b [7,15]. Oxidation of the annealed Al_8 HEA resulted in

the formation of Al_2O_3, $(Al+Cr)_2O_3$, and an Fe+Cr+Ni-rich spinel, as shown by the plan-view and cross-sectional BSE images in Figure 3c,d. Spinel phases of this type are commonly observed on M–Cr–Al alloys during the initial stages of oxidation [30].

Figure 3e,f show plan-view and cross-sectional BSE images for the as-cast Al_{15} HEA after oxidation [7,15]. An external $NiCr_2O_4$ spinel formed on top of an underlying layer of Cr_2O_3. Additionally, an internal scale of semi-continuous Al_2O_3 was observed directly below the Cr_2O_3 scale. AlN precipitates were also observed beneath the internal Al_2O_3 scale. These nitrides are consistent with the observations of Zhang et al. [22] who reported the formation of AlN precipitates in $Al_{0.5}$FeCoCrNi and $Al_{0.5}$CoCrFeNiSi$_{0.2}$ HEAs oxidized in air at 900 °C. Oxidation of the annealed Al_{15} HEA resulted in the formation of Al_2O_3 with an underlying Fe+Cr+Ni-rich spinel, Figure 3g,h. Similar observations have been reported in austenitic Fe–Ni–Cr–Al alloys [50].

Figure 3i,j show plan-view and cross-sectional BSE images for the as-cast Al_{30} HEA after 50 h of oxidation [7,15]. An external Cr_2O_3 scale formed above an underlying, continuous scale of Al_2O_3. In this particular case, no spinel was observed and very few AlN precipitates were present, Figure 3j. Oxidation of the annealed Al_{30} HEA resulted in the sole formation of Al_2O_3, Figure 3k,l. In contrast to the Al_8 and Al_{15} HEAs, no internal oxidation was observed.

To verify the post oxidation phases in the annealed/oxidized HEAs, XRD analysis was done in plan-view on bulk specimens. Figure 4a shows representative XRD patterns for the annealed HEAs after 50 h of oxidation. Each alloy contained peaks associated with a combination of Al_2O_3, spinel ($NiCr_2O_4$), and FCC, BCC, and/or B2 type phases. Additionally, some peaks associated with Cr_2O_3 were present and are likely associated with the Cr-rich regions observed in some regions of the Al_2O_3 scales.

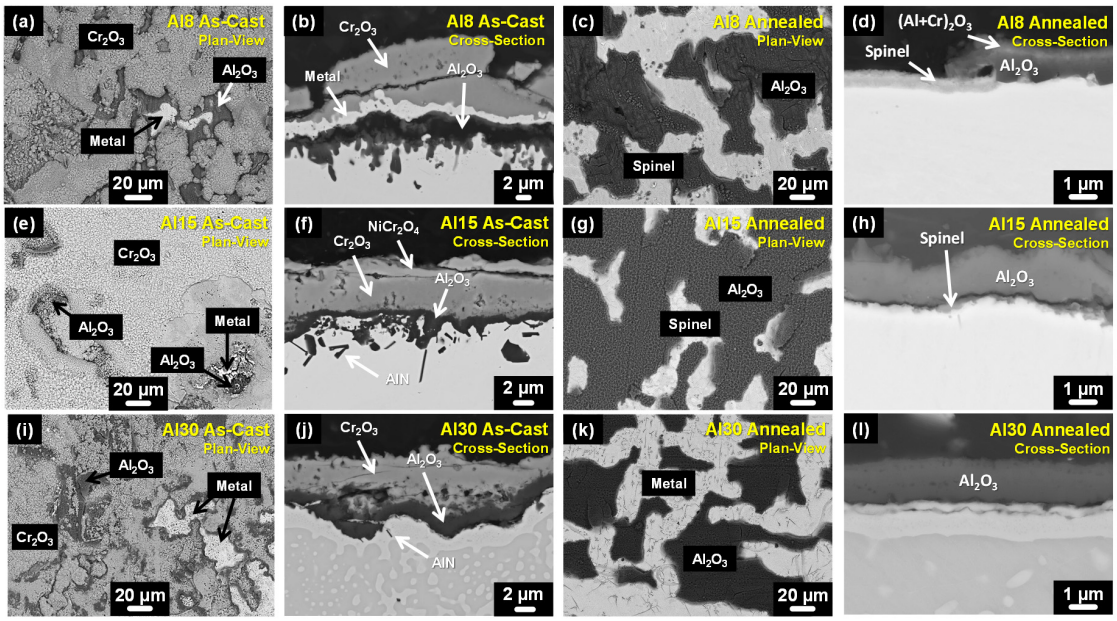

Figure 3. Plan-view and cross-sectional BSE micrographs for the as-cast and annealed Al_8 (**a**–**d**); Al_{15} (**e**–**h**); and Al_{30} (**i**–**l**) HEAs after 50 h of oxidation at 1050 °C.

3.3. Oxidation Behavior

The relative mass changes for the as-cast/oxidized and annealed/oxidized HEAs are shown in Figure 4b. Each of the as-cast and annealed HEAs exhibited some degree of transient oxidation that transitioned to parabolic oxide growth after approximately 5 to 15 h depending on the alloy composition. The behaviors were comparable to those of various Ni–Cr–Al alloys and some wrought Ni-based superalloys [7,30,51]. The as-cast Al_{15} and Al_{30} HEAs appeared to plateau after 30 h and

10 h, respectively. As expected, the highest Al content HEA, Al_{30}, exhibited the smallest mass change. The parabolic oxide growth constants (k_P) for each HEA are shown in Table 3. All of the values were between those reported for model Group II and Group III Ni–Cr–Al alloys [30]. There were only small variations in values between the as-cast and annealed conditions, which is surprising since the post oxidation microstructures were quite different. However, the oxidation behaviors indicate that all of the HEAs exhibit some degree of oxidation resistance.

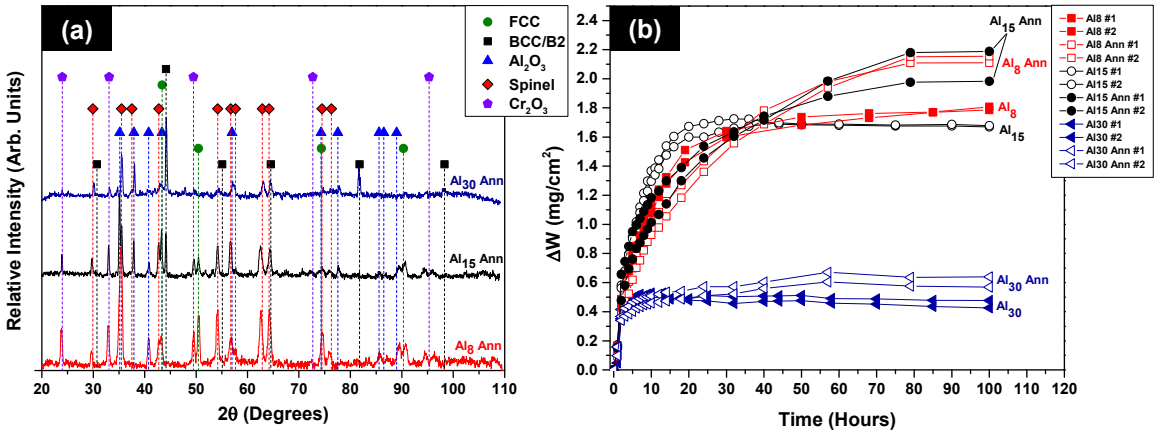

Figure 4. XRD patterns for the annealed HEAs after 50 h of oxidation at 1050 °C in air (**a**); and normalized mass change curves for the as-cast/oxidized and annealed/oxidized HEAs (**b**).

Table 3. Parabolic oxide rate constants (k_P) calculated for the as-cast and annealed HEAs.

Alloy	Initial Condition	k_P (1) ($g^2/cm^4 \cdot s$)	Duration for k_P (1)	k_P (2) ($g^2/cm^4 \cdot s$)	Duration for k_P (2)	Primary Oxides
Al_8	**As-cast**	$\sim 2.5 \times 10^{-11}$	1–30 h	$\sim 2.5 \times 10^{-12}$	30–100 h	Cr_2O_3/Al_2O_3
	Annealed	$\sim 2.2 \times 10^{-11}$	1–40 h	$\sim 8.9 \times 10^{-12}$	40–80 h	Al_2O_3/Spinel
Al_{15}	**As-cast**	$\sim 4.7 \times 10^{-11}$	2–18 h	$\sim 4.2 \times 10^{-12}$	19–36 h	Cr_2O_3/Al_2O_3
	Annealed	$\sim 2.4 \times 10^{-11}$	2–20 h	$\sim 7.8 \times 10^{-12}$	20–80 h	Al_2O_3/Spinel
Al_{30}	**As-cast**	$\sim 1.9 \times 10^{-12}$	2–10 h	—	—	Cr_2O_3/Al_2O_3
	Annealed	$\sim 3.3 \times 10^{-12}$	2–10 h	$\sim 9.1 \times 10^{-13}$	10–60 h	Al_2O_3

4. Discussion

As reported in [7,15], the as-cast HEAs were found to exhibit post-oxidation microstructures indicative of the sequential oxidation reported for model Group II and Group III Ni–Cr–Al alloys [30,52]. Neglecting transient oxide formation, Cr_2O_3 tends to form first, and evolves in tandem with Al_2O_3 formation. Based on the microstructural observations, one can infer that increasing the Al content of the as-cast HEAs enhances the oxidation resistance by promoting the formation of a more-continuous Al_2O_3 scale with/without Cr_2O_3 in contrast to forming a discontinuous, internal Al_2O_3 scale at low Al concentrations. This is not the case for the annealed HEAs, which formed a combination of predominantly Al_2O_3 and spinel phases. Interestingly, in most cases, the spinel phase was observed to form beneath the outer Al_2O_3 scale. Since the phase chemistries between the as-cast and annealed HEAs were not significantly different, the change in oxidation mechanism is most likely related to the relative phase fractions and morphologies.

Annealing was found to alter both of these characteristics promoting increased phase fractions of the Ni+Al-rich B2 phase in all three HEAs. It is proposed that this increased phase fraction and the associated more uniform distribution of the B2 phase within the microstructure provided a larger Al reservoir near the alloy surfaces, creating a more favorable condition for the formation of Al_2O_3.

Delaunay et al. [50] demonstrated that the oxidation resistance of austenitic Fe–Ni–Cr–Al alloys could be improved by annealing the alloys to induce precipitation of the B2 β–NiAl phase. During prolonged oxidation exposure, the Al_2O_3 scale depletes the underlying alloy of Al resulting in near surface regions with relatively high concentrations of Fe, Co, and Cr. It is suggested that once the Al content is depleted to a critical level so that the favorability of Al_2O_3 formation is diminished, the formation of the underlying spinel phase takes precedence. The slightly higher mass gain exhibited by the annealed alloys, most prominently at longer oxidation times, can be explained by the formation of the spinel phase, which does not provide oxidation resistance. The spinel phase was not observed in the annealed Al_{30} HEA because the Al content, in comparison to the Al_8 and Al_{15} HEAs, was likely high enough to sustain Al_2O_3 formation, thus suppressing the formation of spinel.

5. Conclusions

The influences of pre-oxidation annealing on the microstructures and oxidation behaviors of three AlCoCrFeNi HEAs were investigated. The following conclusions can be drawn:

(1) The as-cast Al_8 and Al_{15} HEAs consisted of a combination of FCC, BCC, and B2 solid solution phases. Annealing at 1050 °C for 120 h resulted in significant coarsening of the FCC and B2 phases and dissolution of the primary BCC phase. The as-cast Al_{30} HEA consisted of a uniform distribution of sub-micron sized BCC precipitates with spherical morphologies dispersed in a B2 matrix. Annealing of the Al_{30} HEA also caused substantial microstructural coarsening and the formation of additional nano-scale B2 precipitates inside the BCC phase. In all cases, annealing increased the phase fraction of the B2 phase at the expense of the FCC and/or BCC phases.

(2) Discontinuous, isothermal oxidation tests at 1050 °C showed the as-cast HEAs to oxidize in the same way as model Group II and Group III Ni–Cr–Al alloys, with the initial formation of transient oxides and external Cr_2O_3, followed by the development of an internal Al_2O_3 scale. As expected, increased Al concentrations led to enhanced oxidation resistances. In contrast, the annealed HEAs tended to form external Al_2O_3 scales during oxidation with or without underlying spinel phases depending upon Al content. The change in oxidation mechanism was attributed to the increased phase fraction of Ni+Al-rich B2 phase. It is suggested that the enhanced distribution of B2 phase near the alloy free surfaces promoted the formation of Al_2O_3 and thus modifying the subsequent stages of oxidation.

(3) The parabolic oxidation behaviors of all of the HEAs in both the as-cast and annealed states indicate various levels of protection. The calculated parabolic oxide growth rate constants (k_P) for all of the HEAs correspond to those expected for Group II and Group III Ni–Cr–Al alloys. Although annealing had a large impact on the post oxidation microstructures, it seemed to have lesser influence on the parabolic growth rate constants.

Acknowledgments: This work utilized equipment owned by the Central Analytical Facility (CAF), which is housed at the University of Alabama. The authors also acknowledge partial support from the National Science Foundation under grant DMR-1411280.

Author Contributions: For this work, Todd Butler and Mark Weaver both worked together to conceive and design the experiments performed. Todd Butler and Mark Weaver both participated in the synthesis of the alloys studied in this work. Todd Butler individually conducted the oxidation tests and performed all analytical characterization. Both Todd Butler and Mark Weaver equally participated in the writing and revision process (including figures) for this paper. In this manner, both Todd Butler and Mark Weaver have contributed substantially to the work reported.

Conflicts of Interest: The authors declare no conflict of interest.

References

1. Miracle, D.B.; Miller, J.D.; Senkov, O.N.; Woodward, C.; Uchic, M.D.; Tiley, J. Exploration and development of high entropy alloys for structural applications. *Entropy* **2014**, *16*, 494–525. [CrossRef]
2. Yeh, J.-W. Alloy design strategies and future trends in high-entropy alloys. *JOM* **2013**, *65*, 1759–1771. [CrossRef]
3. Yeh, J.W.; Chen, Y.L.; Lin, S.J.; Chen, S.K. High-entropy alloys—A new era of exploitation. *Mater. Sci. Forum* **2007**, *560*, 1–9. [CrossRef]
4. Zhang, Y.; Zuo, T.T.; Tang, Z.; Gao, M.C.; Dahmen, K.A.; Liaw, P.K.; Lu, Z.P. Microstructures and properties of high-entropy alloys. *Prog. Mater. Sci.* **2014**, *61*, 1–93. [CrossRef]
5. Tang, Z.; Huang, L.; He, W.; Liaw, P.K. Alloying and processing effects on the aqueous corrosion behavior of high-entropy alloys. *Entropy* **2014**, *16*, 895–911. [CrossRef]
6. Butler, T.M.; Alfano, J.P.; Martens, R.L.; Weaver, M.L. High-temperature oxidation behavior of Al-Co-Cr-Ni-(Fe or Si) multicomponent high-entropy alloys. *JOM* **2015**, *67*, 246–259. [CrossRef]
7. Butler, T.M.; Weaver, M.L. Oxidation behavior of arc melted AlCoCrFeNi multi-component high entropy alloys. *J. Alloys Compd.* **2016**, *674*, 229–244. [CrossRef]
8. Chang, S.-Y.; Li, C.-E.; Huang, Y.-C.; Hsu, H.-F.; Yeh, J.-W.; Lin, S.-J. Structural and thermodynamic factors of suppressed interdiffusion kinetics in multi-component high-entropy materials. *Sci. Rep.* **2014**, *4*, 4162. [CrossRef] [PubMed]
9. Tsai, K.Y.; Tsai, M.H.; Yeh, J.W. Sluggish diffusion in Co–Cr–Fe–Mn–Ni high-entropy alloys. *Acta Mater.* **2013**, *61*, 4887–4897. [CrossRef]
10. Dąbrowa, J.; Kucza, W.; Cieślak, G.; Kulik, T.; Danielewski, M.; Yeh, J.-W. Interdiffusion in the fcc-structured Al-Co-Cr-Fe-Ni high entropy alloys: Experimental studies and numerical simulations. *J. Alloys Compd.* **2016**, *674*, 455–462. [CrossRef]
11. Zhang, H.; He, Y.-Z.; Pan, Y.; Guo, S. Thermally stable laser cladded CoCrCuFeNi high-entropy alloy coating with low stacking fault energy. *J. Alloys Compd.* **2014**, *600*, 210–214. [CrossRef]
12. Schuh, B.; Martin, F.M.; Volker, B.; George, E.P.; Clemens, H.; Pippan, R.; Hohenwarter, A. Mechanical properties, microstructure and thermal stability of a nanocrystalline CoCrFeMnNi high-entropy alloy after severe plastic deformation. *Acta Mater.* **2015**, *96*, 258–268. [CrossRef]
13. Praveen, S.; Basu, J.; Kashyap, S.; Kottada, R.S. Exceptional resistance to grain growth in nanocrystalline CoCrFeNi high entropy alloy at high homologous temperatures. *J. Alloys Compd.* **2016**, *662*, 361–367. [CrossRef]
14. Liu, Y.-X.; Cheng, C.-Q.; Shang, J.-L.; Wang, R.; Li, P.; Zhao, J. Oxidation behavior of high-entropy alloys Al_xCoCrFeNi (x = 0.15, 0.4) in supercritical water and comparison with hr3c steel. *Trans. Nonferr. Met. Soc. China* **2015**, *25*, 1341–1351. [CrossRef]
15. Butler, T.M.; Weaver, M.L. Investigation of the microstructures and oxidation behavior of AlNiCoCrFe high-entropy alloys. In Proceedings of the Contributed Papers from Materials Science & Technology (MS&T) 2015, Columbus, OH, USA, 4–8 October 2015; TMS: Columbus, OH, USA, 2015; pp. 1257–1264.
16. Jiang, J.; Luo, X. High temperature oxidation behaviour of AlCuTiFeNiCr high-entropy alloy. *Adv. Mater. Res.* **2013**, *652–654*, 1115–1118. [CrossRef]
17. Laplanche, G.; Volkert, U.F.; Eggeler, G.; George, E.P. Oxidation behavior of the CrMnFeCoNi high-entropy alloy. *Oxid. Met.* **2016**, *85*, 629–645. [CrossRef]
18. Chang, Y.-J.; Yeh, A.-C. The evolution of microstructures and high temperature properties of $Al_xCo_{1.5}CrFeNi_{1.5}Ti_y$ high entropy alloys. *J. Alloys Compd.* **2015**, *653*, 379–385. [CrossRef]
19. Tsao, T.-K.; Yeh, A.-C.; Kuo, C.-M.; Murakami, H. High temperature oxidation and corrosion properties of high entropy superalloys. *Entropy* **2016**, *18*, 62. [CrossRef]
20. Chen, S.-T.; Tang, W.-Y.; Kuo, Y.-F.; Chen, S.-Y.; Tsau, C.-H.; Shun, T.-T.; Yeh, J.-W. Microstructure and properties of age-hardenable $Al_xCrFe_{1.5}MnNi_{0.5}$ alloys. *Mater. Sci. Eng. A* **2010**, *527*, 5818–5825. [CrossRef]
21. Yang, H.H.; Tsai, W.T.; Kuo, J.C. Effect of pre-oxidation on increasing resistance of Fe-Al-Ni-Cr-Co-Mn high entropy alloys to molten al attack. *Corros. Eng. Sci. Technol.* **2014**, *49*, 124–129. [CrossRef]
22. Zhang, H.; Wang, Q.T.; Tang, Q.H.; Dai, P.Q. High temperature oxidation property of $Al_{0.5}$FeCoCrNi($Si_{0.2}$, $Ti_{0.5}$) high entropy alloys. *Corros. Prot.* **2013**, *34*, 561–565.

23. Daoud, H.M.; Manzoni, A.M.; Volkl, R.; Wanderka, N.; Glatzel, U. Oxidation behavior of $Al_8Co_{17}Cr_{17}Cu_8Fe_{17}Ni_{33}$, $Al_{23}Co_{15}Cr_{23}Cu_8Fe_{15}Ni_{15}$, and $Al_{17}Co_{17}Cr_{17}Cu_{17}Fe_{17}Ni_{17}$ compositionally complex alloys (high-entropy alloys) at elevated temperatures in air. *Adv. Eng. Mater.* **2015**, *17*, 1134–1141. [CrossRef]
24. Holcomb, G.R.; Tylczak, J.; Carney, C. Oxidation of CoCrFeMnNi high entropy alloys. *JOM* **2015**, *67*, 2326–2339. [CrossRef]
25. Kai, W.; Li, C.C.; Cheng, F.P.; Chu, K.P.; Huang, R.T.; Tsay, L.W.; Kai, J.J. The oxidation behavior of an equimolar FeCoNiCrMn high-entropy alloy at 950 °C in various oxygen-containing atmospheres. *Corros. Sci.* **2016**, *108*, 209–214. [CrossRef]
26. Senkov, O.N.; Senkova, S.V.; Dimiduk, D.M.; Woodward, C.; Miracle, D.B. Oxidation behavior of a refractory $NbCrMo_{0.5}Ta_{0.5}TiZr$ alloy. *J. Mater. Sci.* **2012**, *47*, 6522–6534. [CrossRef]
27. Gorr, B.; Azim, M.; Christ, H.J.; Mueller, T.; Schliephake, D.; Heilmaier, M. Phase equilibria, microstructure, and high temperature oxidation resistance of novel refractory high-entropy alloys. *J. Alloys Compd.* **2015**, *624*, 270–278. [CrossRef]
28. Gorr, B.; Mueller, F.; Christ, H.J.; Mueller, T.; Chen, H.; Kauffmann, A.; Heilmaier, M. High temperature oxidation behavior of an equimolar refractory metal-based alloy 20Nb-20Mo-20Cr-20Ti-20Al with and without Si addition. *J. Alloys Compd.* **2016**, *688*, 468–477. [CrossRef]
29. Liu, C.M.; Wang, H.M.; Zhang, S.Q.; Tang, H.B.; Zhang, A.L. Microstructure and oxidation behavior of new refractory high entropy alloys. *J. Alloys Compd.* **2014**, *583*, 162–169. [CrossRef]
30. Giggins, C.S.; Pettit, F.S. Oxidation of Ni-Cr-Al alloys between 1000 °C and 1200 °C. *J. Electrochem. Soc.* **1971**, *118*, 1782–1790. [CrossRef]
31. Tang, Q.H.; Huang, Y.; Huang, Y.Y.; Liao, X.Z.; Langdon, T.G.; Dai, P.Q. Hardening of an $Al_{0.3}CoCrFeNi$ high entropy alloy via high-pressure torsion and thermal annealing. *Mater. Lett.* **2015**, *151*, 126–129. [CrossRef]
32. Wang, W.-R.; Wang, W.-L.; Yeh, J.-W. Phases, microstructure and mechanical properties of $Al_xCoCrFeNi$ high-entropy alloys at elevated temperatures. *J. Alloys Compd.* **2014**, *589*, 143–152. [CrossRef]
33. Manzoni, A.; Daoud, H.; Völkl, R.; Glatzel, U.; Wanderka, N. Phase separation in equiatomic AlCoCrFeNi high-entropy alloy. *Ultramicroscopy* **2013**, *132*, 212–215. [CrossRef] [PubMed]
34. Zhang, C.; Zhang, F.; Chen, S.; Cao, W. Computational thermodynamics aided high-entropy alloy design. *JOM* **2012**, *64*, 839–845. [CrossRef]
35. Wang, W.-R.; Wang, W.-L.; Wang, S.-C.; Tsai, Y.-C.; Lai, C.-H.; Yeh, J.-W. Effects of al addition on the microstructure and mechanical property of $Al_xCoCrFeNi$ high-entropy alloys. *Intermetallics* **2012**, *26*, 44–51. [CrossRef]
36. Huang, J.C. Evaluation of tribological behavior of Al-Co-Cr-Fe-Ni high entropy alloys using molecular dynamics simulation. *Scanning* **2012**, *34*, 325–331. [CrossRef] [PubMed]
37. Zhu, J.M.; Fu, H.M.; Zhang, H.F.; Wang, A.M.; Li, H.; Hu, Z.Q. Microstructure and compressive properties of multiprincipal component $AlCoCrFeNiCu_x$ alloys. *J. Alloys Compd.* **2011**, *509*, 3476–3480. [CrossRef]
38. Kao, Y.-F.; Chen, T.-J.; Chen, S.-K.; Yeh, J.-W. Microstructure and mechanical property of as-cast, -homogenized, and -deformed $Al_xCoCrFeNi$ ($0 \leq x \leq 2$) high-entropy alloys. *J. Alloys Compd.* **2009**, *488*, 57–64. [CrossRef]
39. Wang, Y.P.; Li, B.S.; Ren, M.X.; Yang, C.; Fu, H.Z. Microstructure and compressive properties of AlCrFeCoNi high entropy alloy. *Mater. Sci. Eng. A* **2008**, *491*, 154–158. [CrossRef]
40. Tang, Z.; Senkov, O.N.; Parish, C.M.; Zhang, C.; Zhang, F.; Santodonato, L.J.; Wang, G.; Zhao, G.; Yang, F.; Liaw, P.K. Tensile ductility of an AlCoCrFeNi multi-phase high-entropy alloy through hot isostatic pressing (hip) and homogenization. *Mater. Sci. Eng. A* **2015**, *647*, 229–240. [CrossRef]
41. Zhou, Y.J.; Zhang, Y.; Wang, Y.L.; Chen, G.L. Solid solution alloys of $AlCoCrFeNiTi_x$ with excellent room-temperature mechanical properties. *Appl. Phys. Lett.* **2007**, *90*, 181904. [CrossRef]
42. Li, D.; Zhang, Y. The ultrahigh charpy impact toughness of forged $Al_xCoCrFeNi$ high entropy alloys at room and cryogenic temperatures. *Intermetallics* **2016**, *70*, 24–28. [CrossRef]
43. Munitz, A.; Salhov, S.; Hayun, S.; Frage, N. Heat treatment impacts the micro-structure and mechanical properties of AlCoCrFeNi high entropy alloy. *J. Alloys Compd.* **2016**, *683*, 221–230. [CrossRef]
44. Saunders, N.; Miodownik, A.P. *Calphad (Calculation of Phase Diagrams): A Comprehensive Guide*; Pergamon Press: Oxford, UK, 1998; p. 479.

45. Andersson, J.O.; Helander, T.; Hoglund, L.; Shi, P.; Sundman, B. Thermo-calc and dictra, computational tools for materials science. *Calphad* **2002**, *26*, 273–312. [CrossRef]
46. *Thermocalc*, version 2015a; ThermoCalc Software AB: Stckholm, Sweden, 2015.
47. *Thermocalc Ni-Based Superalloys Database*, version TCNI8; ThermoCalc Software AB: Stockholm, Sweden, 2015.
48. Tomus, D.; Ng, H.P. In situ lift-out dedicated techniques using FIB–sem system for tem specimen preparation. *Micron* **2013**, *44*, 115–119. [CrossRef] [PubMed]
49. German, R.M. *Powder Metallurgy & Particular Materials Processing*; Metal Powder Industries Federation: Princeton, NJ, USA, 2005; p. 528.
50. Delaunay, D.; Huntz, A.M. Influence of structural parameters on oxidation of austenitic Fe-Ni-Cr-Al alloys. *J. Mater. Sci.* **1983**, *18*, 189–194. [CrossRef]
51. Jang, C.; Kim, D.; Kim, D.; Sah, I.; Ryu, W.-S.; Yoo, Y.-S. Oxidation behaviors of wrought nickel-based superalloys in various high temperature environments. *Trans. Nonferr. Met. Soc. China* **2011**, *21*, 1524–1531. [CrossRef]
52. Birks, N.; Meier, G.H.; Pettit, F.S. *High-Temperature Oxidation of Metals*, 2nd ed.; Cambridge University Press: Cambridge, UK, 2006.